ACS APPLIED MATERIALS & INTERFACES

www.acsami.org

Research Article

Electrochemical Oxidation of Metal–Catechol Complexes as a New Synthesis Route to the High-Quality Ternary Photoelectrodes: A Case Study of Fe_2TiO_5 Photoanodes

Dongho Lee,[‖] Valentin Urena Baltazar,[‖] Tyler J. Smart, Yuan Ping,* and Kyoung-Shin Choi*

Cite This: *ACS Appl. Mater. Interfaces* 2020, 12, 29275–29284

Read Online

ACCESS | Metrics & More | Article Recommendations | Supporting Information

ABSTRACT: A new electrochemical, solution-based synthesis method to prepare uniform multinary oxide photoelectrodes was developed. This method involves solubilizing multiple metal ions as metal–catechol complexes in a pH condition where they are otherwise insoluble. When some of the catechol ligands are electrochemically oxidized, the remaining metal complexes become insoluble and are deposited as metal–catechol films on the working electrode. The resulting films are then annealed to form crystalline multinary oxide electrodes. Because catechol can serve as a complexing agent for a variety of metal ions, the newly developed method can be used to prepare a variety of multinary oxide films. In the present study, we used this method to prepare n-type Fe_2TiO_5 photoanodes and investigated their photoelectrochemical properties for use in a photoelectrochemical water-splitting cell. We also performed a computational investigation with two goals. The first goal was to investigate small electron polaron formation in Fe_2TiO_5. Charge transport in most oxide photoelectrodes involves small polaron hopping, but small polaron formation in Fe_2TiO_5 has not been examined prior to this work. The second goal was to investigate the effect of substitutional Sn doping at the Fe site on the electronic band structure and the carrier concentration of Fe_2TiO_5. The combined experimental and theoretical results presented in this study greatly improve our understanding of Fe_2TiO_5 for use as a photoanode.

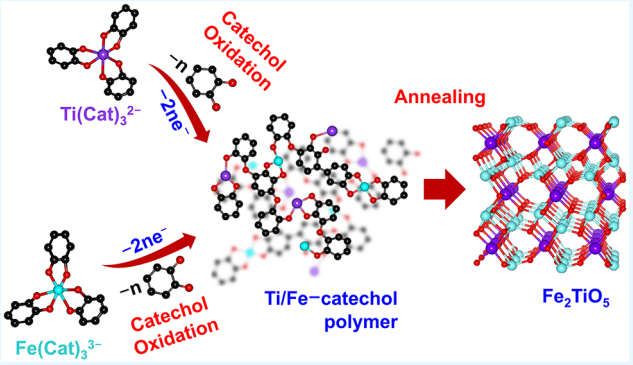

KEYWORDS: *Fe_2TiO_5, electrodeposition, catechol, photoanode, ternary oxide, solar water splitting, photoelectrochemical cell*

1. INTRODUCTION

Photoelectrochemical water-splitting cells utilize solar energy to split water to produce hydrogen fuel.[1−3] A key component in the photoelectrochemical cell is the semiconductor photoelectrode that absorbs photons and generates photo-excited mobile charge carriers to drive the water reduction and oxidation reactions.[4] To date, intensive work has been done to identify efficient photoelectrodes. While past studies mainly focused on investigating the photoelectrochemical properties of photoelectrodes with simple compositions such as binary oxides (i.e., Fe_2O_3, WO_3, and TiO_2), recent studies have focused more on the development of photoelectrodes with more complex compositions (i.e., ternary oxides).[5] By mixing two different metal ions in oxide matrices, ternary oxides offer numerous ways to change the atomic and electronic structures of binary oxides, which can result in superior photo-electrochemical properties. For example, the ternary oxide Fe_2TiO_5 does not possess the major limitations of its parent binary oxides, Fe_2O_3 and TiO_2. Fe_2O_3 has a relatively narrow band gap energy of 2.1 eV, but one of its major limitations is the position of its conduction band minimum (CBM), which is 200 mV more positive than the water reduction potential.[4,6] TiO_2 has a suitable CBM for water reduction, but its band gap is very wide (3.2 eV).[7] On the other hand, Fe_2TiO_5 has both a narrow band gap of 2.1 eV and a CBM that is more negative than the water reduction potential.[8−10]

One major difficulty in evaluating ternary oxide photo-electrodes is that it is challenging to prepare them as pure, uniform electrodes. This is because the parent binary oxides are often thermodynamically more stable than the desired ternary oxide, meaning that the binary oxides can easily form as impurity phases and negatively affect the uniformity of the ternary composition throughout the film. Thus, developing a general synthesis method that can produce a variety of ternary oxides as high-quality photoelectrodes would be immensely beneficial.

Received: March 22, 2020
Accepted: June 3, 2020
Published: June 18, 2020

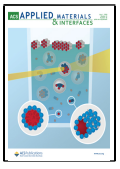

https://dx.doi.org/10.1021/acsami.0c05359
ACS Appl. Mater. Interfaces 2020, 12, 29275–29284

In this study, we report a new synthesis method based on the electrochemical oxidation of catechol. Catechol can serve as a complexing agent to solubilize various metal ions (e.g., Fe^{3+}, V^{4+}, Mn^{3+}, Cu^{2+}, Co^{2+}, Ni^{2+}, Zn^{2+}, Mn^{2+}, Al^{3+}, and Ti^{4+}) in pH conditions where they are otherwise insoluble.[11,12] Thus, electrochemical oxidation of the catechol ligands in a plating solution containing multiple metal ions solubilized by catechol ligands can offer an elegant way to produce various multinary oxides containing these metal ions as uniform films via a solution-based process. Previously, spontaneous oxidation of metal−catechol complexes by O_2 in air has been used to form a protective coating on a pyrite (FeS_2) surface to prevent its dissolution.[13] In follow-up studies, the oxidation mechanisms of various metal−catechol complexes were investigated electrochemically.[12,14−16] However, prior to our work, the oxidation of metal−catechol complexes has not been utilized as a strategy to form multinary metal oxide films via coprecipitation of metal−catechol complexes containing two or more different metal ions.

Here, we demonstrate the use of the electrochemical oxidation of catechol for the synthesis of Fe_2TiO_5 photoelectrodes as an example. Fe_2TiO_5 was selected for two reasons. First, because Fe_2O_3 and TiO_2 are both very stable and unreactive binary oxides, the ability to synthesize high-quality Fe_2TiO_5 using our new method demonstrates the method's efficacy. Second, as mentioned above, Fe_2TiO_5 has many advantageous features for use as a photoanode; however, investigations of this compound as a single photoanode have been limited.[8,17−21] Therefore, the synthesis of high-quality Fe_2TiO_5 electrodes also provides us with a great opportunity to systematically examine the photoelectrochemical properties of Fe_2TiO_5. Furthermore, we note that although there have been a few theoretical studies on the electronic structure of pristine Fe_2TiO_5,[22−24] polaron formation and the effect of doping on the charge-transport properties of Fe_2TiO_5 have not been theoretically investigated. For this reason, we also performed computational investigations on Fe_2TiO_5 regarding its polaron formation and the effect of a dopant on polaron formation and carrier density. The combined experimental and theoretical results presented in this study will offer an in-depth understanding of Fe_2TiO_5 for use as a photoanode.

2. EXPERIMENTAL SECTION

2.1. Materials. Catechol (Alfa Aesar, 99%), titanium(IV) bis(ammonium lactato)dihydroxide (TALH) solution (Sigma-Aldrich, 50 wt % in H_2O), 15 mM $Fe(NO_3)_3{\cdot}9H_2O$ (Sigma-Aldrich, ≥98%), NaOH (Sigma-Aldrich, 97%), $Ni(NO_3)_2{\cdot}6H_2O$ (Acros, 99%), 2-methoxyethanol (Sigma-Aldrich, 99.8%), KOH (Sigma-Aldrich, 85%), $NaNO_3$ (Sigma-Aldrich, 99%), and Na_2SO_3 (Sigma-Aldrich, ≥98%) were used without further purification. Unless otherwise specified, deionized (DI) water (Barnstead E-pure water purification system, resistivity > 18 MΩ cm) was used to prepare all solutions.

2.2. Preparation of Fe_2TiO_5 Electrodes. Electrodeposition was carried out in a three-electrode undivided cell using a VMP2 multichannel potentiostat (Princeton Applied Research). Fluorine-doped tin oxide (FTO) (Hartford Glass) was used as the working electrode (WE), an Ag/AgCl (4 M KCl) electrode was used as the reference electrode (RE), and platinum was used as the counter electrode (CE). The lateral dimensions of the FTO WE used in this study were 1.0 cm × 1.2 cm. The platinum CE was prepared by depositing a 100 nm platinum layer on top of a 30 nm titanium adhesion layer by e-beam evaporation on a cleaned glass slide.

The plating solution was 40 mL of an aqueous solution containing 67.5 mM catechol, 12.5 mM TALH, and 15 mM $Fe(NO_3)_3{\cdot}9H_2O$. TALH and $Fe(NO_3)_3{\cdot}9H_2O$ were sequentially added to the catechol solution, and then, the pH was raised to 8 using NaOH. In this solution, all Ti^{4+} and Fe^{3+} ions were solubilized by catechol, and no precipitation was observed upon the pH increase. The dominant metal−catechol species in the plating solution were predicted from the speciation diagram plotted by the Hyperquad Simulation and Speciation (Hyss) software.[25] Equations and thermodynamic values such as formation and solubility constants used to create the plots are listed in the Supporting Information (Tables S1 and S2).

To deposit Ti/Fe−catechol films onto the WE, a potentiostatic deposition was carried out by applying 0.34 V versus Ag/AgCl to the WE and passing 0.1 C/cm^2. Typically, the deposition takes ∼2 min. As-deposited electrodes were rinsed with DI water and blow-dried with air. The resulting electrode was converted to crystalline Fe_2TiO_5 by annealing at 650 °C for 1 h in air (ramping rate = 5 °C/min), followed by natural cooling to room temperature. Finally, the Fe_2TiO_5 film was additionally treated by microwave annealing for 2 min 30 s in a microwave oven (AmazonBasics, 700 W) on 5 g of a packed graphite powder (Sigma-Aldrich, <20 μm) susceptor in a 100 mL Pyrex beaker.[26] When the microwave annealing was used as the only annealing step, the catechol in the film could not be completely removed and carbon residues were left behind. For the preparation of a dense Fe_2TiO_5 electrode, the aforementioned deposition was repeated twice on the same WE before the first annealing process described above. Between each deposition cycle, the film was heated at 400 °C for 5 min on a hot plate to remove the majority of catechol so that the voids generated by the removal of catechol could be filled by the subsequent depositions. The removal of catechol was indicated by a change of the film color from black to pale orange.

2.3. Loading of Ni_2FeO_x Oxygen Evolution Catalyst. To load the Ni_2FeO_x oxygen evolution catalyst (OEC) onto the Fe_2TiO_5 electrode, 100 μL/cm^2 of a solution of 6.66 mM $Ni(NO_3)_2{\cdot}6H_2O$ and 3.33 mM $Fe(NO_3)_3{\cdot}9H_2O$ in 2-methoxyethanol was drop-cast onto the electrode. After drying in air, the electrode was heated in an oven at 70 °C for 5 min and rinsed with 0.1 M KOH for 10 s before photoelectrochemical measurements.[18]

2.4. Materials Characterization. The dominant metal−catechol species in the plating solution were determined by ultraviolet−visible (UV−vis) spectrophotometric measurements (Varian, Cary 300 UV−vis spectrophotometer). The morphology of the Fe_2TiO_5 electrodes was examined using the LEO 1530 scanning electron microscope (Gemini) at an accelerating voltage of 5 kV. Elemental composition was characterized with the same scanning electron microscope equipped with an UltraDry energy dispersive X-ray spectroscopy (EDS) detector (Thermo Fischer Scientific) at an accelerating voltage of 20 kV. The crystallinity and purity were confirmed with the D8 ADVANCE powder X-ray diffractometer (Bruker) using Ni-filtered Cu Kα-radiation with λ = 1.5418 Å. Absorbances of the electrodes were determined from the Cary 5000 ultraviolet−visible−near infrared (UV−vis−NIR) spectrophotometer (Agilent) with an integrating sphere to simultaneously collect reflectance and transmittance from the electrodes. Surface chemical states of the electrodes were investigated by using a K-Alpha X-ray photoelectron spectrometer (XPS, Thermo Scientific). A monochromatized Al Kα X-ray (1486.6 eV) was used as the excitation source with a pass energy of 30 eV. The binding energies were calibrated with respect to the adventitious C 1s peak at 284.8 eV.

2.5. Photoelectrochemical and Electrochemical Characterization. Photoelectrochemical and electrochemical measurements were carried out in an undivided three-electrode cell using an SP-200 potentiostat (Bio-Logic). Fe_2TiO_5 was used as the WE, Pt was used as the CE, and because all measurements were performed in strongly basic conditions capable of dissolving a glass frit, a Hg/HgO (1 M NaOH) RE was used instead of the Ag/AgCl RE. The measured potential versus the RE was converted to potential versus the reversible hydrogen electrode (RHE) using the equation below.

$$E(\text{vs RHE}) = E(\text{vs Hg/HgO}) + E_{\text{Hg/HgO}}(\text{reference}) + 0.0591\ \text{V} \times \text{pH} \qquad (E_{\text{Hg/HgO}}(\text{reference}) = 0.140\ \text{V vs NHE at 25 °C})$$

https://dx.doi.org/10.1021/acsami.0c05359
ACS Appl. Mater. Interfaces 2020, 12, 29275−29284

Simulated solar light was generated using an LCS-100 solar simulator (Oriel) equipped with a 150 W Xe arc lamp and an air mass 1.5 global (AM 1.5G) filter. An infrared filter (Newport) and a focusing lens were placed between the light source and the electrode, and the intensity of light was calibrated to 1 sun (100 mW/cm^2) at the back side of the FTO substrate using an NREL-certified GaAs reference cell (PV measurement). Photoelectrochemical $J-V$ and $J-t$ measurements were taken in 1 M NaOH (pH 13.6). For sulfite oxidation, 1 M Na_2SO_3 was added to the 1 M NaOH solution. Capacitance measurements for Mott–Schottky plots were obtained using the same three-electrode system, but the Fe_2TiO_5 WE was masked with an electroplating tape 370 (3M) to expose a circular geometric area of 0.2 cm^2. 1 M NaOH was used as the electrolyte, and a sinusoidal modulation of 10 mV was applied at frequencies of 0.5–2 kHz.

2.6. Computational Methods. All density functional theory (DFT) calculations were performed with the Quantum ESPRESSO[27] package using the PBE + U exchange correlation functional, ultrasoft pseudopotentials,[28] and Hubbard U parameters of 4.3 eV on Fe 3d states[29] and 3.0 eV on Ti 3d states. This choice of U parameters gives an electronic band gap of 2.00 eV, which is in good agreement with the experimental band gap of 2.1 eV.[8,23] The orthorhombic 32 atom unit cell of the pseudobrookite Fe_2TiO_5 structure (space group $Ccmm$) was used and then expanded to a 1 × 3 × 1 supercell with 96 atoms. The antiferromagnetic magnetic structure was chosen with respect to the lowest energy spin isomer, as determined by other studies.[24] A k-point grid of 2 × 2 × 2 was used for the supercell calculation with a wavefunction kinetic energy cutoff of 40 Ry and a k-point grid of 8 × 8 × 8 for the projected density of states (PDOS). All Sn doping calculations were conducted by replacing a single Fe atom with a Sn atom in the 96-atom supercell that contained 24 Fe atoms. This corresponds to replacing 4.2 at. % Fe with Sn. We applied a newly developed charge correction scheme[30] to calculations containing excess charge, as implemented in the JDFTx package.[31]

Theoretical absorption spectra for both pristine and Sn-doped Fe_2TiO_5 were calculated from the imaginary part of the dielectric function obtained from the YAMBO[32] code in the random phase approximation with local field effects. The input YAMBO single-particle eigenvalues and wave functions were obtained from the DFT + U calculations done with Quantum ESPRESSO.[27] The absorption coefficient (α) is related to the real and imaginary parts of dielectric function (ϵ_1 and ϵ_2, respectively) via the following equation.[33]

$$\alpha(\omega) = \frac{\omega}{c}\frac{\epsilon_2(\omega)}{\sqrt{\frac{\epsilon_1(\omega) + \sqrt{\epsilon_1(\omega)^2 + \epsilon_2(\omega)^2}}{2}}}$$

3. RESULTS AND DISCUSSION

3.1. Experimental Study. *3.1.1. New Electrochemical Synthesis Method Using Metal–Catechol Precursors.* The plating solution used in this study was an aqueous catechol solution (pH 8) containing TALH as the Ti^{4+} source and $Fe(NO_3)_3{\cdot}9H_2O$ as the Fe^{3+} source. Without catechol, Ti^{4+} and Fe^{3+} are insoluble in neutral aqueous media, as shown in their speciation diagrams (Figure 1a,b). When catechol serves as a complexing agent, Ti^{4+} is solubilized as a tris-catecholate ($Ti(Cat)_3^{2-}$) and Fe^{3+} is solubilized as di- and tris-catecholates ($Fe(Cat)_2^-$ and $Fe(Cat)_3^{3-}$, respectively) in neutral media (Figure 1c,d). The spectroscopic detection of these metal–catechol species and the details of the measurement conditions can be found in Figure S1.

As the solubilization of Ti^{4+} and Fe^{3+} is enabled only by the formation of metal–catechol complexes with the appropriate number of catechol ligands, oxidizing catechol ligands to make catechol-deficient complexes results in the precipitation of insoluble metal–catechol complexes. Because electrochemical oxidation of catechol occurs only on the WE, the precipitation will occur only on the WE, forming a film. For example, when $Ti(Cat)_3^{2-}$ loses one or two catechol ligands by electrochemical catechol oxidation, the resulting $Ti(Cat)_2$ and/or $Ti(Cat)^{2+}$ species are insoluble and will form a film on the WE (Scheme 1a).[14] In the same manner, Fe–catechol films can be deposited when soluble $Fe(Cat)_2^-$ and $Fe(Cat)_3^{3-}$ species lose one or two catechol molecules by electrochemical catechol oxidation and form insoluble $Fe(Cat)^+$ (Scheme 1b).[11] The linear sweep voltammograms of $Ti(Cat)_3^{2-}$ and $Fe(Cat)_3^{3-}$ showing the oxidation of catechol ligands can be found in Figure S2. We note that during catechol oxidation, in addition to the two-electron oxidation of catechol to quinone, one-electron oxidation can also occur to form a semiquinone radical, which can cross-link multiple metal–catechol complexes and form metal–catechol polymers (Figure S3).[34]

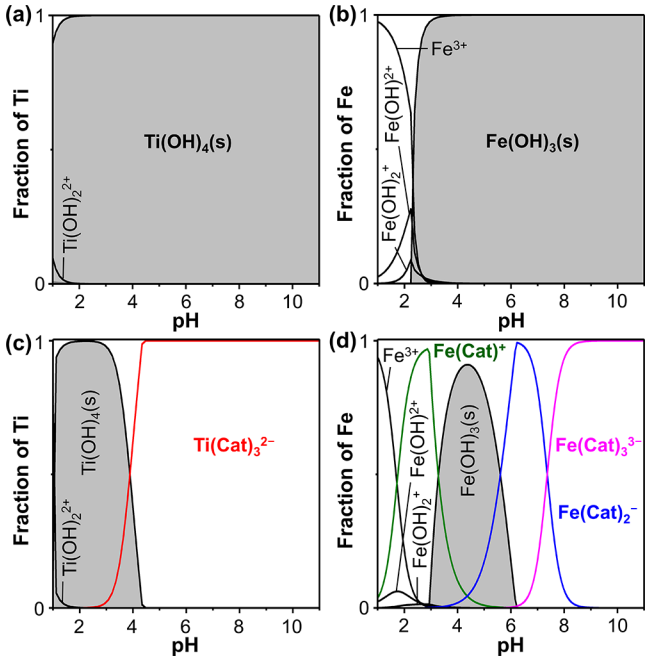

Figure 1. Speciation diagrams of metal–catechol complexes: (a) Ti-only; (b) Fe-only; (c) Ti–catechol; and (d) Fe–catechol systems; where [Ti^{4+}] = 12.5 mM, [Fe^{3+}] = 15 mM, and [Cat] = 67.5 mM. The regions where insoluble $Ti(OH)_4(s)$ and $Fe(OH)_3(s)$ form are shown in gray. The concentrations of Ti^{4+}, Fe^{3+}, and catechol used in these speciation diagrams are the same as those used in the plating solution.

Because the deposition of films is triggered not by the reduction or oxidation of the Ti or Fe ions that have different redox potentials but by the oxidation of the catechol ligands, Ti and Fe can be codeposited uniformly at the same potential without forming Ti-rich or Fe-rich domains (Figure S4). As a result, high-quality, uniform Fe_2TiO_5 films can be obtained after annealing, which removes catechol molecules and induces solid-state reactions (Figure 2). A desired Ti/Fe ratio in the film can be obtained by adjusting the Ti/Fe ratio in the plating solution.

3.1.2. Characterization of the Fe_2TiO_5 Electrode. Scanning electron microscopy (SEM) images of the electrodeposited films before and after annealing are shown in Figure 3a,b along with their photographs. The as-deposited Ti/Fe–catechol polymer film shows a dense, featureless morphology. During the annealing process, catechol species are oxidized to CO_2 while Fe_2TiO_5 forms by a solid-state reaction, resulting in a

https://dx.doi.org/10.1021/acsami.0c05359
ACS Appl. Mater. Interfaces 2020, 12, 29275–29284

Scheme 1. Reaction Pathways of (a) Ti−Catechol and (b) Fe−Catechol Complexes[a]

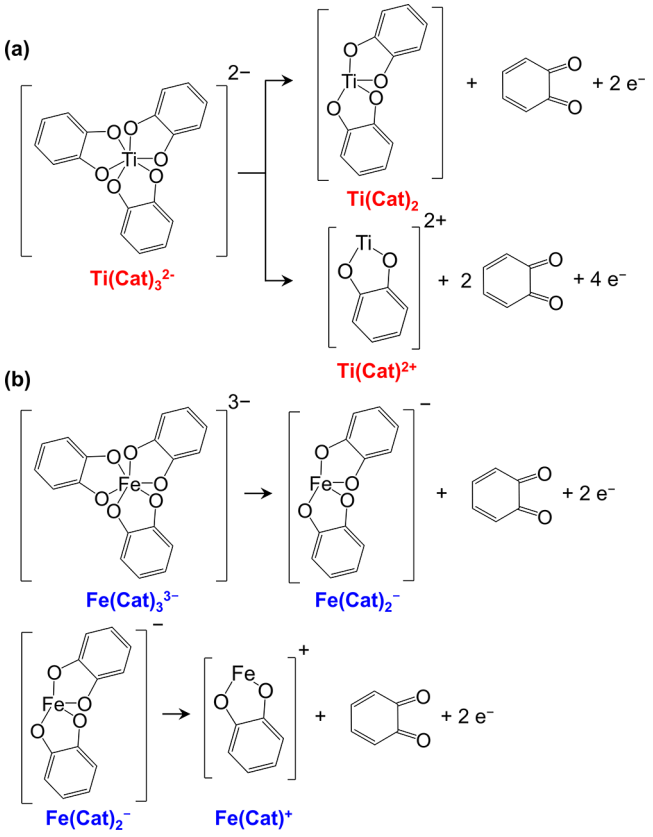

[a]Water molecules (or hydroxides) that are coordinated to Ti^{4+} or Fe^{3+} were omitted for simplicity.

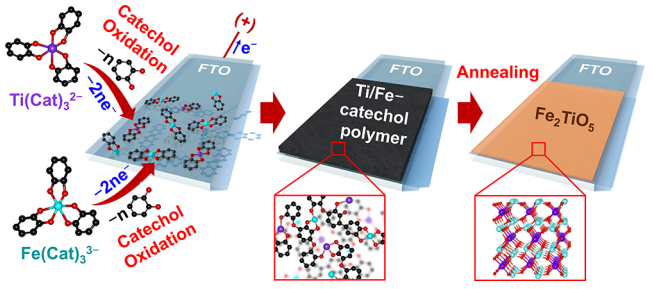

Figure 2. Schematic diagram for the preparation of Fe_2TiO_5 on an FTO substrate by the oxidation of metal−catechol complexes.

film with porous, nanocrystalline morphology. The thickness of the Fe_2TiO_5 film was estimated to be ~75 nm from a side-view SEM image (Figure 3c). The color of the film changed from black to pale orange after annealing. The X-ray diffraction (XRD) pattern of the film after annealing confirmed that pure, crystalline Fe_2TiO_5 was formed (Figure 3d). [For comparison, the as-deposited Ti/Fe−catechol polymer film is amorphous (Figure S5).] The UV−vis absorption spectrum of the Fe_2TiO_5 electrode shows a band gap of ~2.1 eV (Figure 3e), which agrees with the previously reported band gap of Fe_2TiO_5.[8,23]

3.1.3. Photoelectrochemical Properties of the Fe_2TiO_5 Electrode. The photoelectrochemical properties of the Fe_2TiO_5 electrode were first investigated by measuring the photocurrent generated for sulfite oxidation in 1 M NaOH containing 1 M Na_2SO_3 sulfite (Figure 4a). Sulfite is a hole scavenger with extremely fast hole injection kinetics.[35] Therefore, the loss of surface-reaching holes to surface recombination can be assumed to be negligible during sulfite oxidation. As a result, the photocurrent measurement for sulfite oxidation can generally allow us to estimate the number of surface-reaching holes and the photoelectrochemical properties of a photoanode that are not affected by its poor water oxidation kinetics.[35] The Fe_2TiO_5 electrode generated anodic photocurrent under illumination, confirming that it is n-type and can serve as a photoanode. The photocurrent onset potential was 0.58 V versus RHE, and the photocurrent density at 1.23 V versus RHE was 0.35 mA/cm^2.

We note that the annealing process used in this study was composed of two steps. The first step was to anneal at 650 °C for 1 h in air, and the second step was to microwave anneal for 2 min 30 s using a packed graphite powder susceptor. Without the additional microwave annealing, the photocurrent at 1.23 V versus RHE was only 0.26 mA/cm^2. The use of microwave annealing for the preparation of Fe_2TiO_5 has been reported in previous studies.[18,21,36] However, because these studies did not directly compare photoelectrochemical properties with and without microwave annealing, the exact effect of microwave annealing on the photoelectrochemical properties of Fe_2TiO_5 was not elucidated. Thus, we conducted a further investigation to identify the reasons why microwave annealing enhances the photocurrent of Fe_2TiO_5.

The SEM images, XRD patterns, and UV−vis spectra of Fe_2TiO_5 before and after microwave annealing showed that the microwave annealing did not change the morphology, crystallinity, or photon absorption of Fe_2TiO_5 (Figure S6). However, Mott−Schottky plots show that the microwave annealing increased the carrier density and shifted the flatband potential slightly to the negative direction, judging from a decrease in the slopes and a shift of the *x*-intercepts to the negative direction, respectively (Figure 4b,c).[35] These results indicate an increase in carrier density during the microwave annealing, which improved the majority carrier charge-transport properties, reducing bulk electron−hole recombination in Fe_2TiO_5. The most common defect that can serve as a donor in n-type oxides when no extrinsic impurity is intentionally introduced is the oxygen vacancy. However, it is unlikely that microwave annealing in air can increase the amount of oxygen vacancies in Fe_2TiO_5. Thus, the most plausible explanation for the observed change is that Sn^{4+} from the FTO substrate migrates into Fe_2TiO_5 and serves as an electron donor. In fact, when graphite is used as a susceptor during microwave annealing as in our microwave annealing process, it is known that the temperature of the sample can increase up to 750 °C.[37] Also, it was previously reported that when Fe_2O_3 films on an FTO substrate were annealed at temperatures of 750−800 °C or microwave annealed, Sn^{4+} from FTO diffused into the Fe_2O_3 lattice, forming Sn-doped Fe_2O_3,[38−41] which resulted in an increase in photocurrent generation.

We investigated whether the presence of Sn in Fe_2TiO_5 after microwave annealing could be detected by X-ray photoelectron spectroscopy (XPS). Unfortunately, the Sn XPS spectrum of Fe_2TiO_5 showed Sn 3d peaks even before the microwave annealing because the Fe_2TiO_5 electrode used in this study is porous and some of the bare FTO substrate remains exposed. This made it difficult to differentiate the Sn peaks originating from Sn incorporated into the Fe_2TiO_5 electrode from those

https://dx.doi.org/10.1021/acsami.0c05359
ACS Appl. Mater. Interfaces 2020, 12, 29275−29284

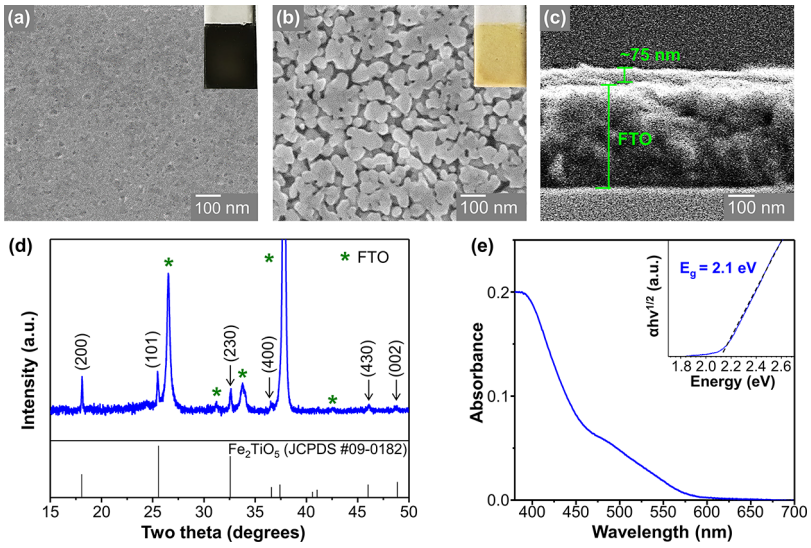

Figure 3. Top-view SEM images of (a) as-deposited Ti/Fe−catechol polymer films and (b) Fe_2TiO_5 films obtained after annealing; (c) side-view SEM image of the Fe_2TiO_5 film; (d) XRD pattern and (e) UV−vis absorption spectrum of the Fe_2TiO_5 film. The inset in (e) shows the Tauc plot for the determination of an indirect band gap of the Fe_2TiO_5 film.

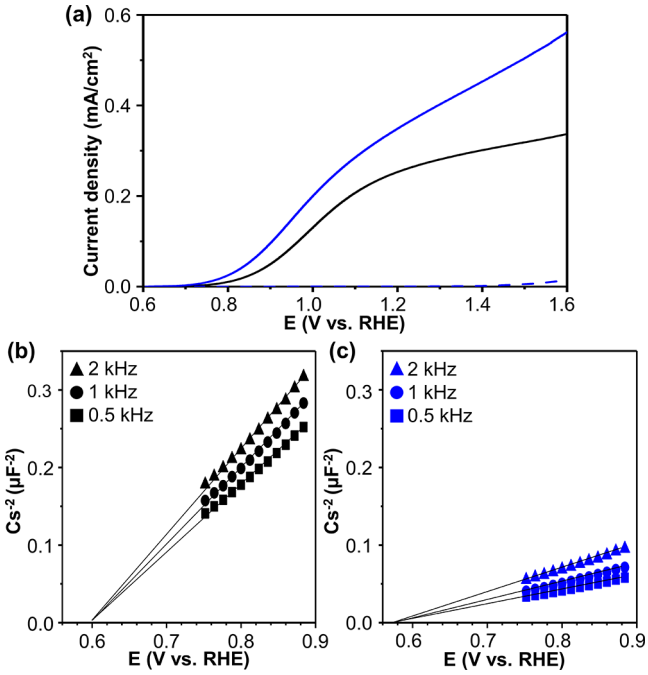

Figure 4. (a) $J-V$ plot for sulfite oxidation before (black) and after (blue) microwave annealing. The blue dashed line corresponds to the dark current of the microwave-annealed Fe_2TiO_5 film. The photocurrent was measured in 1 M NaOH containing 1 M Na_2SO_3 (pH 13.6) (AM 1.5 G, 100 mW/cm^2 illumination). Mott−Schottky plots (b) before and (c) after microwave annealing measured in 1 M NaOH (pH 13.6) using multiple frequencies (0.5−2 kHz).

originating from the FTO substrate. In order to resolve this issue, the synthesis conditions were modified to prepare a thicker and denser Fe_2TiO_5 electrode (Figure S7a) so that the Sn peaks from the FTO substrate would be negligible (Figure 5a). The photocurrent generated from the resulting thicker Fe_2TiO_5 electrode was lower than that of the original electrode (Figure S7b) because the severe bulk recombination, which is a known issue for Fe_2TiO_5,[8,17] outweighed the increased photon absorption of the thicker film. Because the thickness of the original film was optimized to maximize the photocurrent generation, a further increase in thickness resulted in decreased photocurrent. Nonetheless, after the microwave annealing, the thicker film also showed an increase in photocurrent generation (Figure S7b), meaning that these thicker films show the same phenomenon that was observed in the original film and can therefore be used to elucidate the cause of photocurrent enhancement in the microwave-annealed films.

The XPS analysis of the thicker film showed that the intensity of the Sn $3d_{5/2}$ peaks gradually increased with the microwave annealing time (Figure 5a). As XPS is a surface technique and can detect Sn present only at the surface, this result clearly confirms that Sn^{4+} from the underlying FTO substrate can diffuse through the entire Fe_2TiO_5 electrode. We also found that while the positions of the Fe 2p peaks agree well with those expected for Fe^{3+}, upon incorporation of Sn^{4+}, a satellite peak appeared at a binding energy of 716 eV, which is indicative of the presence of Fe^{2+} (Figure 5b).[38,42,43] Unlike the Fe 2p spectra, the Ti 2p spectra showed no changes upon microwave annealing (Figure 5c). These results suggest that the extra electrons gained from Sn^{4+} doping are localized on Fe^{3+} atoms forming Fe^{2+} ions. This postulation is confirmed by the DFT calculations discussed later in the Computational Study section.

As discussed above, because of the severe bulk recombination in Fe_2TiO_5, increasing film thickness could not further increase photocurrent. Unfortunately, the photon absorption achieved by a thin Fe_2TiO_5 film was not considerable, as shown in Figure 3e. One way to further increase the absorbance of Fe_2TiO_5 without creating more bulk recombination is to stack multiple thin films whose individual thickness was optimized for maximum photocurrent generation.[44] The absorbance and photocurrent of four films stacked in parallel are shown in Figure 6a,b, where the absorbance at 400 nm was increased from 0.17 to 0.39 and the photocurrent for sulfite oxidation at 1.23 V versus RHE was increased from 0.35 to 0.85 mA/cm^2. After stacking four films, more films did not result in any additional increase in absorbance or photocurrent because the combined absorption, reflection, and scattering of four films made the intensity of the transmitted light from the

https://dx.doi.org/10.1021/acsami.0c05359
ACS Appl. Mater. Interfaces 2020, 12, 29275−29284

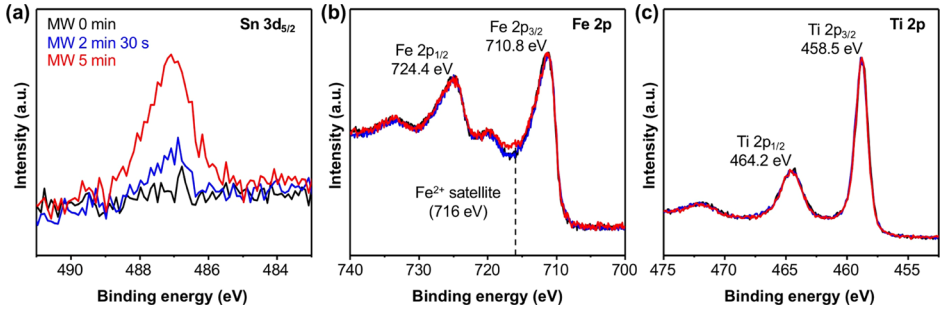

Figure 5. (a) Sn $3d_{5/2}$, (b) Fe 2p, and (c) Ti 2p XPS spectra of the thicker Fe_2TiO_5 electrode prepared with different microwave annealing times: 0 min (black), 2 min 30 s (blue), and 5 min (red).

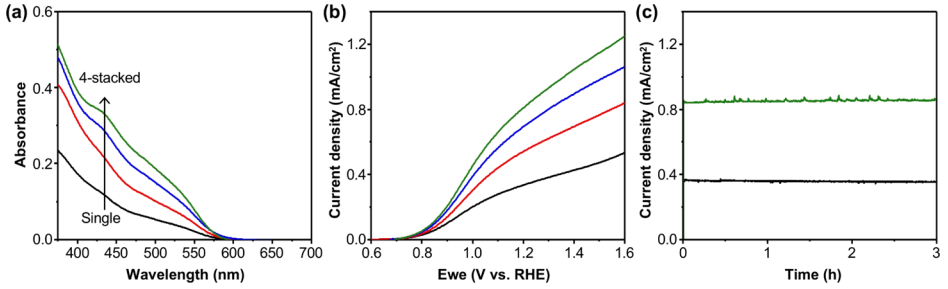

Figure 6. (a) UV−vis absorbance of the single (black), two-stacked (red), three-stacked (blue), and four-stacked (green) Fe_2TiO_5 electrodes; (b) *J*−*V* plots and (c) *J*−*t* plots at 1.23 V vs RHE measured in 1 M NaOH containing 1 M Na_2SO_3 (pH 13.6). All measurements were obtained with AM 1.5 G, 100 mW/cm^2 illumination.

fourth film negligible. The *J*−*t* plots of a single Fe_2TiO_5 photoanode and up to four stacked photoanodes confirmed the chemical and photoelectrochemical stability of Fe_2TiO_5 in 1 M NaOH containing Na_2SO_3 (Figure 6c).

Last, photoelectrochemical water oxidation by the Fe_2TiO_5 electrodes was also examined (Figure 7a). When used without an OEC, the photocurrent generated by Fe_2TiO_5 for water oxidation was approximately 50% of the photocurrent generated for sulfite oxidation. However, when Ni_2FeO_x was added on the Fe_2TiO_5 surface as an OEC, the photocurrent for water oxidation increased to ∼80% of the photocurrent generated for sulfite oxidation. The *J*−*t* plot at 1.23 V versus RHE showed stable photocurrent generation, demonstrating the photoelectrochemical stability of the Ni_2FeO_x-modified Fe_2TiO_5 electrode during water oxidation in 1 M NaOH solution (Figure 7b).

3.2. Computational Study. *3.2.1. Small Polaron Formation.* Because of strong electron−phonon interactions, carriers in many transition metal oxides are trapped by their self-induced lattice distortions, forming small polarons.[45] These small electron polarons are important in understanding the charge-transport properties of oxide photoanodes because charge transport in these photoanodes occurs via a thermally activated polaron hopping mechanism.[46] However, prior to this work, the formation of small electron polarons in Fe_2TiO_5 had not been investigated. Thus, we first investigated the formation of small electron polarons in Fe_2TiO_5 by introducing an extra electron into pristine Fe_2TiO_5.

When an extra electron was introduced into the neutral pristine Fe_2TiO_5 structure, we found that this excess charge localizes on an Fe site and forms a small electron polaron, lowering the oxidation state of the Fe from Fe^{3+} to Fe^{2+}. In the pristine Fe_2TiO_5, the Fe^{3+} site is octahedrally coordinated, resulting in the O_h crystal field splitting of $3d^5$ states. The d electrons occupy both the e_g and t_{2g} states with a high-spin

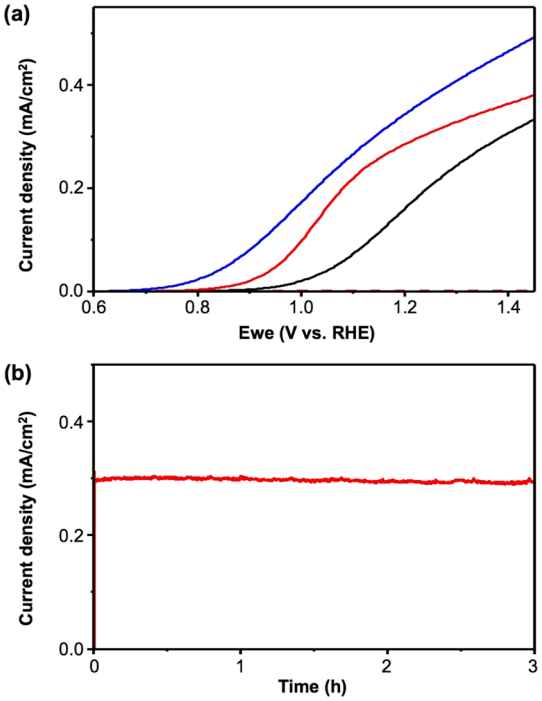

Figure 7. (a) *J*−*V* plots for sulfite oxidation by Fe_2TiO_5 (blue) and water oxidation by Fe_2TiO_5 (black) and Fe_2TiO_5/Ni_2FeO_x (red). The red dashed line along the *x*-axis corresponds to the dark current for water oxidation by Fe_2TiO_5/Ni_2FeO_x. (b) *J*−*t* plots for water oxidation by the Fe_2TiO_5/Ni_2FeO_x electrode at 1.23 V vs RHE. The electrolyte was 1 M NaOH (pH 13.6). 1 M Na_2SO_3 was added for sulfite oxidation. All measurements were obtained with AM 1.5 G, 100 mW/cm^2 illumination.

configuration. The newly added electron thus occupies a lower energy t_{2g} state with the opposite spin. The norm-squared

https://dx.doi.org/10.1021/acsami.0c05359
ACS Appl. Mater. Interfaces 2020, 12, 29275−29284

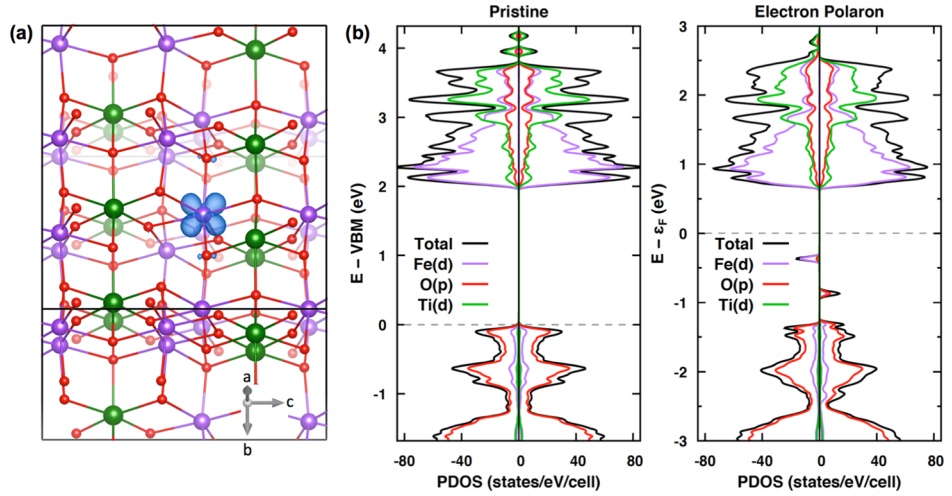

Figure 8. (a) Norm-squared wavefunction for the spin-down electron polaron (blue cloud) shown as an isosurface in the Fe_2TiO_5 lattice (green = Ti, purple = Fe, and red = O). Isosurface value is 3% of the maximum amplitude of the wavefunction; (b) PDOS of Fe_2TiO_5 before (left) and after (right) a single electron polaron is introduced in a 96-atom supercell.

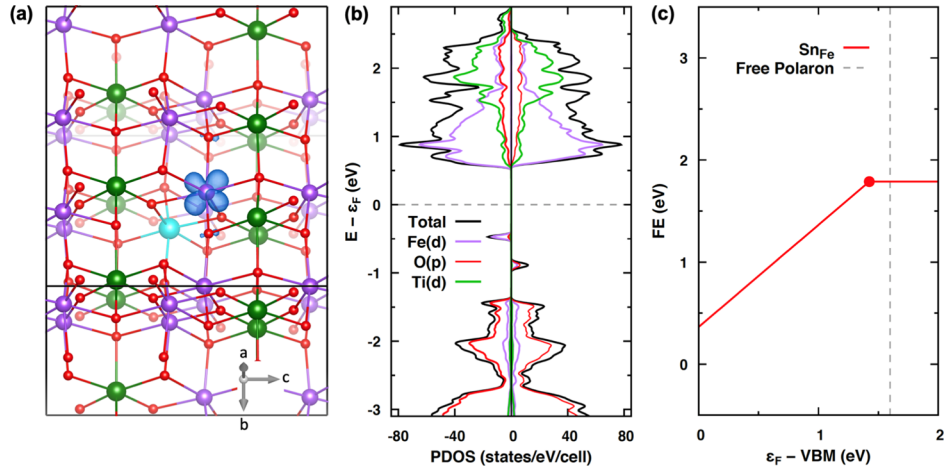

Figure 9. (a) Norm-squared wavefunction of the electron polaron (blue cloud) formed in Fe_2TiO_5 with a single Sn dopant introduced into a 96-atom supercell (green = Ti, purple = Fe, turquoise blue = Sn, and red = O). Isosurface value is 3% of the maximum amplitude of the wavefunction; (b) PDOS for Sn-doped Fe_2TiO_5; (c) charge FE diagram of Sn in Fe_2TiO_5.

polaron wavefunction consistent with the t_{2g} symmetry (d_{xz}) is shown in Figure 8a.

PDOS of Fe_2TiO_5 before and after the addition of the extra electron are shown in Figure 8b. After the addition of the extra electron, the polaron state formed at 1.00 eV below the CBM. This polaron state is mainly composed of the Fe t_{2g} character (Figure 8a). There is also a perturbed valence state formed 0.40 eV above the valence band maximum (VBM), which is generated by the formation of Fe^{2+} perturbing the valence states. This state has both Fe 3d (e_g) and O 2p character. The norm-squared wavefunction of the perturbed valence state is shown in Figure S8a.

3.2.2. Electronic Structure of Sn-Doped Fe_2TiO_5. Because our experimental results indicated that Sn doping caused by the microwave annealing is responsible for the increase in the carrier density of Fe_2TiO_5, we investigated the effect of Sn doping on Fe_2TiO_5 in our Computational Study. We note that substitutional doping of Sn at the Ti site cannot change the carrier concentration in Fe_2TiO_5, as Sn^{4+} and Ti^{4+} have the same charge. However, the substitution of Sn for Fe in the Fe_2TiO_5 lattice results in the introduction of an extra electron into the system because the oxidation state of Sn^{4+} is higher than the native Fe^{3+} site it substitutes. Our computational result shows that the extra electron from a single Sn dopant at the Fe site spontaneously forms a small electron polaron on the nearest Fe site, as shown in Figure 9a. We found that the electron polaron state caused by Sn doping is very similar to that caused by adding one extra electron to pristine Fe_2TiO_5 in terms of both energy level (1.00 eV below the CBM) and contributing orbitals [mainly, Fe 3d (t_{2g})] (Figure 9a,b). Sn doping also resulted in the formation of a perturbed valence state at 0.47 eV above the VBM because of the formation of Fe^{2+} (Figure 9b). As in the case of adding one extra electron to pristine Fe_2TiO_5, this perturbed state mainly possesses Fe 3d (e_g) and O 2p character (Figure S8b).

In order to examine whether the formation of these states by Sn doping affects photon absorption of Fe_2TiO_5, we simulated and compared absorption spectra of pristine and Sn-doped Fe_2TiO_5 (Figure S9). We did not include the effects of excitons in this calculation because they do not change significantly upon doping in most transition-metal oxides.[47−49] The simulated absorption shows small anisotropy after Sn

https://dx.doi.org/10.1021/acsami.0c05359
ACS Appl. Mater. Interfaces 2020, 12, 29275−29284

doping. While the absorption along the (100) and (001) directions is nearly the same as that of the pristine Fe_2TiO_5, the absorption along the (010) direction shows a small peak around 1.5 eV, which is due to the perturbed valence state formed after doping. The fact that no noticeable change in the UV−vis spectrum was observed experimentally upon Sn doping (Figure S6c) suggests that the amount of experimentally achieved Sn doping is less than the amount simulated in the Computational Study. The simulated amount was 4.2 at. % Sn at the Fe site, which corresponds to replacing a single Fe atom with a Sn atom in the 96-atom supercell and was the smallest doping amount achievable for the selected cell.

3.2.3. Sn as a Shallow Donor in Fe_2TiO_5. To examine the effects of the Sn dopant on carrier concentration in Fe_2TiO_5, we considered the charge formation energy (FE) of Sn on an Fe site in the Fe_2TiO_5 system as follows.

$$\mathrm{FE}_q[\varepsilon_\mathrm{F}] = E_q - E_\mathrm{pst} + \sum_i \mu_i \Delta N_i + q\varepsilon_\mathrm{F} + \Delta_q$$

where FE_q is the FE of the Sn dopant at charge q, E_q is the total energy of the defect system with charge q, E_pst is the total energy of the pristine system, ΔN_i is the change in the number of atoms of species i with chemical potential μ_i, ε_F is the Fermi energy, and Δ_q is the charged defect correction as implemented in JDFTx[31] in order to remove the spurious interactions of the charged defect with its periodic images and with the uniform compensating background charge.[30] The value of the Fermi energy at which the system undergoes a transition of charge state q to q' defines the charge transition level $\varepsilon^{q|q'}$

$$\varepsilon^{q|q'} = \frac{E_q^\mathrm{f}[\varepsilon_\mathrm{F}] - E_q^\mathrm{f}[\varepsilon_\mathrm{F}]}{q' - q}$$

For a semiconductor in which the majority carriers are transported through the conduction band, the ionization energy of a donor is defined as the energy difference between its charge transition level and the CBM. Using this definition, the ionization energy of a Sn dopant is ∼0.58 eV and, therefore, the Sn dopant would be considered a deep donor. However, for an oxide semiconductor in which the charge transport involves polaron formation and polaron hopping, the ionization energy of a defect-bound polaron is determined by the energy difference between the charge transition level of the dopant and the energy level of an unbound free polaron (i.e., a polaron far from the defect) in the pristine system.[29,50−52] This free polaron level is defined by the Fermi level corresponding to the $\varepsilon^{0|-1}$ transition in the pristine system with a single polaron. The free polaron level is shown as a gray line, and the $\varepsilon^{+1|0}$ transition of the Sn dopant in the Sn-doped Fe_2TiO_5 system is shown as a red dot in Figure 9c. The ionization energy of a defect-bound polaron in Sn-doped Fe_2TiO_5 was determined to be ∼0.17 eV. This energy is several multiples of kT at room temperature (26 meV); therefore, Sn doping can increase the carrier concentration. This clarifies the role of the Sn dopant in enhancing the majority carrier concentration of Fe_2TiO_5 and is consistent with our experimental findings.

4. CONCLUSIONS

In summary, we demonstrated the electrochemical oxidation of catechol as a new synthesis strategy to prepare high-quality multinary oxide films using Fe_2TiO_5 as an example. A plating solution containing both Ti−catechol and Fe−catechol complexes was used, and coprecipitation of Ti/Fe−catechol complexes on the WE was achieved via the oxidation of a fraction of the catechol ligands that solubilized Ti^{4+} and Fe^{3+} ions. The resulting films were annealed to form crystalline Fe_2TiO_5 photoanodes, and their photoelectrochemical properties were investigated for sulfite oxidation and water oxidation. It was discovered that during microwave annealing, Sn^{4+} from the FTO substrate diffused into the Fe_2TiO_5 lattice and increased the majority carrier density, resulting in an increase in photocurrent generation.

In order to investigate small electron polaron formation and the effect of Sn doping on the electronic band structure of Fe_2TiO_5, we performed a computational investigation on Fe_2TiO_5. Our results showed that an extra electron introduced in the Fe_2TiO_5 lattice forms a small electron polaron localized at the Fe site, decreasing the oxidation state of Fe from +3 to +2. We found that when the Fe^{3+} site of Fe_2TiO_5 is substitutionally doped with Sn^{4+}, the extra electron gained from Sn doping also localizes at the Fe site, forming a small electron polaron. This result agreed well with the experimental XPS result that Sn^{4+} doping results in the formation of Fe^{2+} in Fe_2TiO_5. To examine the effects of the Sn dopant on carrier concentration in Fe_2TiO_5, the ionization energy of a defect-bound polaron was examined. The result showed that Sn dopants at the Fe sites can serve as donors and increase the majority carrier density at room temperature. The combined experimental and computational results clearly explained the effect of Sn doping caused by the microwave annealing and offered a significantly enhanced understanding of Fe_2TiO_5 as a photoanode.

■ ASSOCIATED CONTENT

Supporting Information

The Supporting Information is available free of charge at https://pubs.acs.org/doi/10.1021/acsami.0c05359.

Additional data for metal−catechol complexes including UV−vis spectra and linear sweep voltammograms; additional SEM images, EDS elemental mapping, UV−vis spectra, XRD patterns, and J−V plots of Fe_2TiO_5; norm-squared wavefunction of the perturbed valence states of Fe_2TiO_5 after free polaron formation and Sn doping; and simulated absorption spectra for pristine and Sn-doped Fe_2TiO_5 (PDF).

■ AUTHOR INFORMATION

Corresponding Authors

Yuan Ping − *Department of Chemistry and Biochemistry, University of California, Santa Cruz, California 95064, United States;* orcid.org/0000-0002-0123-3389; Email: yuanping@ucsc.edu

Kyoung-Shin Choi − *Department of Chemistry, University of Wisconsin—Madison, Madison, Wisconsin 53706, United States;* orcid.org/0000-0003-1945-8794; Email: kschoi@chem.wisc.edu

Authors

Dongho Lee − *Department of Chemistry, University of Wisconsin—Madison, Madison, Wisconsin 53706, United States;* orcid.org/0000-0001-8607-9976

Valentin Urena Baltazar − *Department of Chemistry and Biochemistry, University of California, Santa Cruz, California 95064, United States*

https://dx.doi.org/10.1021/acsami.0c05359
ACS Appl. Mater. Interfaces 2020, 12, 29275−29284

Tyler J. Smart − *Department of Physics, University of California, Santa Cruz, California 95064, United States*

Complete contact information is available at: https://pubs.acs.org/10.1021/acsami.0c05359

Author Contributions

[‖]D.L. and V.U.B. authors contributed equally.

Notes

The authors declare no competing financial interest.

■ ACKNOWLEDGMENTS

K.-S.C. acknowledges the financial support by the Division of Chemical Sciences, Geosciences, and Biosciences, Office of Basic Energy Sciences of the U.S. Department of Energy through Grant DE-SC0008707. Y.P. acknowledges the financial support from the National Science Foundation under Grant CHE-1904547. Y.P. used resources of the Center for Functional Nanomaterials, which is a U.S. DOE Office of Science Facility, and the Scientific Data and Computing Center, a component of the Computational Science Initiative, at Brookhaven National Laboratory under contract no. DE-SC0012704. Y.P. also used the lux supercomputer at UC Santa Cruz, funded by NSF MRI Grant AST-1828315, and the Extreme Science and Engineering Discovery Environment (XSEDE), which is supported by National Science Foundation grant number ACI1548562.

■ REFERENCES

(1) Nozik, A. J. Photoelectrochemistry: Applications to Solar Energy Conversion. *Annu. Rev. Phys. Chem.* **1978**, *29*, 189−222.
(2) Walter, M. G.; Warren, E. L.; McKone, J. R.; Boettcher, S. W.; Mi, Q.; Santori, E. A.; Lewis, N. S. Solar Water Splitting Cells. *Chem. Rev.* **2010**, *110*, 6446−6473.
(3) Lewis, N. S.; Crabtree, G.; Nozik, A. J.; Wasielewski, M. R.; Alivisatos, P. Basic Research Needs for Solar Energy Utilization. *Basic Energy Sciences Workshop on Solar Energy Utilization*, Bethesda, MD, April, 2005.
(4) Sivula, K.; van de Krol, R. Semiconducting Materials for Photoelectrochemical Energy Conversion. *Nat. Rev. Mater.* **2016**, *1*, 15010.
(5) Lee, D. K.; Lee, D.; Lumley, M. A.; Choi, K.-S. Progress on Ternary Oxide-Based Photoanodes for Use in Photoelectrochemical Cells for Solar Water Splitting. *Chem. Soc. Rev.* **2019**, *48*, 2126−2157.
(6) Gurudayal; Bassi, P. S.; Sritharan, T.; Wong, L. H. Recent Progress in Iron Oxide Based Photoanodes for Solar Water Splitting. *J. Phys. D: Appl. Phys.* **2018**, *51*, 473002.
(7) Kment, S.; Riboni, F.; Pausova, S.; Wang, L.; Wang, L.; Han, H.; Hubicka, Z.; Krysa, J.; Schmuki, P.; Zboril, R. Photoanodes Based on TiO_2 and α-Fe_2O_3 for Solar Water Splitting − Superior Role of 1D Nanoarchitectures and of Combined Heterostructures. *Chem. Soc. Rev.* **2017**, *46*, 3716−3769.
(8) Bassi, P. S.; Chiam, S. Y.; Gurudayal; Barber, J.; Wong, L. H. Hydrothermal Grown Nanoporous Iron Based Titanate, Fe_2TiO_5 for Light Driven Water Splitting. *ACS Appl. Mater. Interfaces* **2014**, *6*, 22490−22495.
(9) Courtin, E.; Baldinozzi, G.; Sougrati, M. T.; Stievano, L.; Sanchez, C.; Laberty-Robert, C. New Fe_2TiO_5-Based Nanoheterostructured Mesoporous Photoanodes with Improved Visible Light Photoresponses. *J. Mater. Chem. A* **2014**, *2*, 6567−6577.
(10) Deng, J.; Lv, X.; Liu, J.; Zhang, H.; Nie, K.; Hong, C.; Wang, J.; Sun, X.; Zhong, J.; Lee, S.-T. Thin-Layer Fe_2TiO_5 on Hematite for Efficient Solar Water Oxidation. *ACS Nano* **2015**, *9*, 5348−5356.
(11) Sever, M. J.; Wilker, J. J. Visible Absorption Spectra of Metal−Catecholate and Metal−Tironate Complexes. *Dalton Trans.* **2004**, 1061−1072.
(12) Park, I.; Tabelin, C. B.; Seno, K.; Jeon, S.; Ito, M.; Hiroyoshi, N. Simultaneous Suppression of Acid Mine Drainage Formation and Arsenic Release by Carrier-Microencapsulation Using Aluminum-Catecholate Complexes. *Chemosphere* **2018**, *205*, 414−425.
(13) Satur, J.; Hiroyoshi, N.; Tsunekawa, M.; Ito, M.; Okamoto, H. Carrier-Microencapsulation for Preventing Pyrite Oxidation. *Int. J. Miner. Process.* **2007**, *83*, 116−124.
(14) Park, I.; Tabelin, C. B.; Magaribuchi, K.; Seno, K.; Ito, M.; Hiroyoshi, N. Suppression of the Release of Arsenic from Arsenopyrite by Carrier-Microencapsulation Using Ti-Catechol Complex. *J. Hazard. Mater.* **2018**, *344*, 322−332.
(15) Li, X.; Hiroyoshi, N.; Tabelin, C. B.; Naruwa, K.; Harada, C.; Ito, M. Suppressive Effects of Ferric-Catecholate Complexes on Pyrite Oxidation. *Chemosphere* **2019**, *214*, 70−78.
(16) Li, X.; Gao, M.; Hiroyoshi, N.; Tabelin, C. B.; Taketsugu, T.; Ito, M. Suppression of Pyrite Oxidation by Ferric-Catecholate Complexes: An Electrochemical Study. *Miner. Eng.* **2019**, *138*, 226−237.
(17) An, X.; Lan, H.; Liu, R.; Liu, H.; Qu, J. Light Absorption Modulation of Novel Fe_2TiO_5 Inverse Opals for Photoelectrochemical Water Splitting. *New J. Chem.* **2017**, *41*, 7966−7971.
(18) Zhang, H.; Kim, J. H.; Kim, J. H.; Lee, J. S. Engineering Highly Ordered Iron Titanate Nanotube Array Photoanodes for Enhanced Solar Water Splitting Activity. *Adv. Funct. Mater.* **2017**, *27*, 1702428.
(19) Wang, M.; Wu, X.; Huang, K.; Sun, Y.; Zhang, Y.; Zhang, H.; He, J.; Chen, H.; Ding, J.; Feng, S. Enhanced Solar Water-Splitting Activity of Novel Nanostructured Fe_2TiO_5 Photoanode by Electrospray and Surface F-Modification. *Nanoscale* **2018**, *10*, 6678−6683.
(20) Kuang, S.; Wang, M.; Geng, Z.; Wu, X.; Sun, Y.; Ma, W.; Chen, D.; Liu, J.; Feng, S.; Huang, K. Enhancement of Fe_2TiO_5 Photoanode through Surface Al^{3+} Treatment and FeOOH Modification. *ACS Sustain. Chem. Eng.* **2019**, *7*, 14347−14352.
(21) Zhang, H.; Park, S. O.; Joo, S. H.; Kim, J. H.; Kwak, S. K.; Lee, J. S. Precisely-Controlled, a Few Layers of Iron Titanate Inverse Opal Structure for Enhanced Photoelectrochemical Water Splitting. *Nano Energy* **2019**, *62*, 20−29.
(22) Jin, L.; Zhou, C. Electronic Structures and Optic Properties of Fe_2TiO_5 Using LSDA+U Approach. *Prog. Nat. Sci. Mater. Int.* **2013**, *23*, 413−419.
(23) Ngo, H. D.; Ngo, T. D.; Tamanai, A.; Chen, K.; Cuong, N. T.; Handegard, O. S.; Pucci, A.; Umezawa, N.; Nabatame, T.; Nagao, T. Structure and Optical Properties of Sputter Deposited Pseudobrookite Fe_2TiO_5 Thin Films. *CrystEngComm* **2019**, *21*, 34−40.
(24) Petit, S.; Melissen, S. T. A. G.; Duclaux, L.; Sougrati, M. T.; Bahers, T. L.; Sautet, P.; Dambournet, D.; Borkiewicz, O.; Laberty-Robert, C.; Durupthy, O. How Should Iron and Titanium Be Combined in Oxides to Improve Photoelectrochemical Properties? *J. Phys. Chem. C* **2016**, *120*, 24521−24532.
(25) Alderighi, L.; Gans, P.; Ienco, A.; Peters, D.; Sabatini, A.; Vacca, A. Hyperquad Simulation and Speciation (HySS): A Utility Program for the Investigation of Equilibria Involving Soluble and Partially Soluble Species. *Coord. Chem. Rev.* **1999**, *184*, 311−318.
(26) Oghbaei, M.; Mirzaee, O. Microwave versus Conventional Sintering: A Review of Fundamentals, Advantages and Applications. *J. Alloys Compd.* **2010**, *494*, 175−189.
(27) Giannozzi, P.; Baroni, S.; Bonini, N.; Calandra, M.; Car, R.; Cavazzoni, C.; Ceresoli, D.; Chiarotti, G. L.; Cococcioni, M.; Dabo, I.; Corso, A. D.; de Gironcoli, S.; Fabris, S.; Fratesi, G.; Gebauer, R.; Gerstmann, U.; Gougoussis, C.; Kokalj, A.; Lazzeri, M.; Martin-Samos, L.; Marzari, N.; Mauri, F.; Mazzarello, R.; Paolini, S.; Pasquarello, A.; Paulatto, L.; Sbraccia, C.; Scandolo, S.; Sclauzero, G.; Seitsonen, A. P.; Smogunov, A.; Umari, P.; Wentzcovitch, R. M. QUANTUM ESPRESSO: A Modular and Open-Source Software Project for Quantum Simulations of Materials. *J. Phys.: Condens. Matter* **2009**, *21*, 395502.
(28) Garrity, K. F.; Bennett, J. W.; Rabe, K. M.; Vanderbilt, D. Pseudopotentials for High-Throughput DFT Calculations. *Comput. Mater. Sci.* **2014**, *81*, 446−452.

(29) Smart, T. J.; Ping, Y. Effect of Defects on the Small Polaron Formation and Transport Properties of Hematite from First-Principles Calculations. *J. Phys.: Condens. Matter* **2017**, *29*, 394006.
(30) Sundararaman, R.; Ping, Y. First-Principles Electrostatic Potentials for Reliable Alignment at Interfaces and Defects. *J. Chem. Phys.* **2017**, *146*, 104109.
(31) Sundararaman, R.; Letchworth-Weaver, K.; Schwarz, K. A.; Gunceler, D.; Ozhabes, Y.; Arias, T. A. JDFTx: Software for Joint Density-Functional Theory. *SoftwareX* **2017**, *6*, 278−284.
(32) Marini, A.; Hogan, C.; Grüning, M.; Varsano, D. yambo: An Ab Initio Tool for Excited State Calculations. *Comput. Phys. Commun.* **2009**, *180*, 1392−1403.
(33) Jackson, J. D. Classical Electrodynamics; John Wiley & Sons, Inc.: New York, 1999.
(34) Patil, N.; Jérôme, C.; Detrembleur, C. Recent Advances in the Synthesis of Catechol-Derived (Bio)Polymers for Applications in Energy Storage and Environment. *Prog. Polym. Sci.* **2018**, *82*, 34−91.
(35) Govindaraju, G. V.; Wheeler, G. P.; Lee, D.; Choi, K.-S. Methods for Electrochemical Synthesis and Photoelectrochemical Characterization for Photoelectrodes. *Chem. Mater.* **2017**, *29*, 355−370.
(36) Phani, A. R.; Ruggieri, F.; Passacantando, M.; Santucci, S. Low Temperature Growth of Nanocrystalline Fe_2TiO_5 Perovskite Thin Films by Sol-Gel Process Assisted by Microwave Irradiation. *Ceram. Int.* **2008**, *34*, 205−211.
(37) Jang, Y. J.; Jang, J.-W.; Choi, S. H.; Kim, J. Y.; Kim, J. H.; Youn, D. H.; Kim, W. Y.; Han, S.; Lee, J. S. Tree Branch-Shaped Cupric Oxide for Highly Effective Photoelectrochemical Water Reduction. *Nanoscale* **2015**, *7*, 7624−7631.
(38) Ahn, H.-J.; Yoon, K.-Y.; Kwak, M.-J.; Park, J.; Jang, J.-H. Boron Doping of Metal-Doped Hematite for Reduced Surface Recombination in Water Splitting. *ACS Catal.* **2018**, *8*, 11932−11939.
(39) Ahn, H.-J.; Goswami, A.; Riboni, F.; Kment, S.; Naldoni, A.; Mohajernia, S.; Zboril, R.; Schmuki, P. Hematite Photoanode with Complex Nanoarchitecture Providing Tunable Gradient Doping and Low Onset Potential for Photoelectrochemical Water Splitting. *ChemSusChem* **2018**, *11*, 1873−1879.
(40) Zhang, H.; Noh, W. Y.; Li, F.; Kim, J. H.; Jeong, H. Y.; Lee, J. S. Three Birds, One-Stone Strategy for Hybrid Microwave Synthesis of Ta and Sn Codoped Fe_2O_3@$FeTaO_4$ Nanorods for Photo-Electrochemical Water Oxidation. *Adv. Funct. Mater.* **2019**, *29*, 1805737.
(41) Zhang, H.; Lee, J. S. Hybrid Microwave Annealing Synthesizes Highly Crystalline Nanostructures for (Photo)Electrocatalytic Water Splitting. *Acc. Chem. Res.* **2019**, *52*, 3132−3142.
(42) Yamashita, T.; Hayes, P. Analysis of XPS Spectra of Fe^{2+} and Fe^{3+} Ions in Oxide Materials. *Appl. Surf. Sci.* **2008**, *254*, 2441−2449.
(43) Lin, T.-C.; Seshadri, G.; Kelber, J. A. A Consistent Method for Quantitative XPS Peak Analysis of Thin Oxide Films on Clean Polycrystalline Iron Surfaces. *Appl. Surf. Sci.* **1997**, *119*, 83−92.
(44) Kuang, Y.; Jia, Q.; Nishiyama, H.; Yamada, T.; Kudo, A.; Domen, K. A Front-Illuminated Nanostructured Transparent $BiVO_4$ Photoanode for >2% Efficient Water Splitting. *Adv. Energy Mater.* **2016**, *6*, 1501645.
(45) Natanzon, Y.; Azulay, A.; Amouyal, Y. Evaluation of Polaron Transport in Solids from First-Principles. *Isr. J. Chem.* **2020**, *60*, 1−20.
(46) Sharma, S.; Basu, T.; Shahee, A.; Singh, K.; Lalla, N. P.; Sampathkumaran, E. V. Complex Dielectric and Impedance Behavior of Magnetoelectric Fe_2TiO_5. *J. Alloys Compd.* **2016**, *663*, 289−294.
(47) Kim, T. W.; Ping, Y.; Galli, G. A.; Choi, K.-S. Simultaneous Enhancements in Photon Absorption and Charge Transport of Bismuth Vanadate Photoanodes for Solar Water Splitting. *Nat. Commun.* **2015**, *6*, 8769.
(48) Ping, Y.; Galli, G. Optimizing the Band Edges of Tungsten Trioxide for Water Oxidation: A First-Principles Study. *J. Phys. Chem. C* **2014**, *118*, 6019−6028.
(49) Ping, Y.; Rocca, D.; Galli, G. Optical Properties of Tungsten Trioxide from First-Principles Calculations. *Phys. Rev. B: Condens. Matter Mater. Phys.* **2013**, *87*, 165203.
(50) Seo, H.; Ping, Y.; Galli, G. Role of Point Defects in Enhancing the Conductivity of $BiVO_4$. *Chem. Mater.* **2018**, *30*, 7793−7802.
(51) Wheeler, G. P.; Baltazar, V. U.; Smart, T. J.; Radmilovic, A.; Ping, Y.; Choi, K.-S. Combined Theoretical and Experimental Investigations of Atomic Doping to Enhance Photon Absorption and Carrier Transport of $LaFeO_3$ Photocathodes. *Chem. Mater.* **2019**, *31*, 5890−5899.
(52) Smart, T. J.; Pham, T. A.; Ping, Y.; Ogitsu, T. Optical Absorption Induced by Small Polaron Formation in Transition Metal Oxides: The Case of Co_3O_4. *Phys. Rev. Mater.* **2019**, *3*, 102401.

https://dx.doi.org/10.1021/acsami.0c05359
ACS Appl. Mater. Interfaces 2020, 12, 29275−29284